Versatile Airy-Beam Generation Using a 1-Bit Coding Programmable Reflective Metasurface

Rui Feng,[1,2] Badreddine Ratni,[3] Jianjia Yi,[4,†] Kuang Zhang,[5,‡] Xumin Ding,[5] Hailin Zhang,[1] André de Lustrac,[2,6] and Shah Nawaz Burokur[3,*]

[1] *Key Laboratory of Integrated Services Networks, Xidian University, Xi'an, Shaanxi 710071, China*
[2] *Université Paris-Saclay, CNRS, Centre de Nanosciences et de Nanotechnologies, 91120, Palaiseau, France*
[3] *LEME, UPL, Univ Paris Nanterre, F92410 Ville d'Avray, France*
[4] *School of Electronics and Information Engineering, Xi'an Jiaotong University, Xi'an 710049, China*
[5] *Department of Microwave Engineering, Harbin Institute of Technology, Harbin, 150001, China*
[6] *UPL, Univ Paris Nanterre, F92410 Ville d'Avray, France*

(Received 4 April 2020; revised 31 May 2020; accepted 16 June 2020; published 27 July 2020)

The Airy beam, known to present particular unique features, such as diffraction-free, self-healing, and self-bending, has attracted considerable interest in recent years. Here, an electronically controlled reflective coding metasurface is exploited to generate and dynamically manipulate the Airy beam over a wide frequency band in the microwave regime. By judiciously controlling the external dc bias voltage applied to the programmable metasurface, two distinct control states, "0" and "1", are engineered as digital codes for $-\pi/2$ and $+\pi/2$ phase responses, respectively. The programmable binary-phase-coding metasurface enables the generation and active reshaping of the Airy beam to be numerically simulated and experimentally validated. Moreover, the metasurface allows the bandwidth limitation of passive counterparts to be overcome and is able to modulate electromagnetic waves over a broad frequency range, spanning from 9 to 12 GHz, to realize diffraction-free Airy beams.

DOI: 10.1103/PhysRevApplied.14.014081

I. INTRODUCTION

Nondiffracting Airy beams have inspired considerable research interest due to their specific properties. In addition to nondiffracting and self-healing properties, the Airy beam possesses the unique feature of self-acceleration, even without any external potential, compared with the Bessel beam. In 1979, within the context of quantum mechanics, Berry and Balazs [1] theoretically demonstrated that the solution to the Schrödinger equation describing a free particle was in the form of a nondiffracting Airy wave packet. Due to their diffraction-free characteristics, Airy beams carry infinite energy, which was initially difficult, not to say impossible, to demonstrate experimentally. An exponential decaying factor was therefore introduced to truncate the Airy beam for a physical realization [2] and nondiffracting accelerating Airy beams were observed and reported in 2007 by Siviloglou *et al.* [3]. In particular, it is demonstrated that, despite exponential truncation, the Airy beam still exhibits a nondiffracting feature, while its main lobe freely accelerates during propagation along a parabolic trajectory. Since then, the Airy beam has been intensively investigated for its unique properties and potential applications in optical micromanipulation [4–8], laser micromachining [9,10], optical bullet formation [11–14], and microscopy [15–18]. Although most investigations on Airy beams are conducted at optical wavelengths, it may be useful to explore the potential application of such beams in wireless communications in the microwave regime. In particular, the Airy beam is introduced into the radiowave regime for the design of abruptly autofocusing (AAF) beams from antenna arrays [19]. Such beams present the capability of focusing their power right before a target, while maintaining a constant and low maximum intensity along the propagation path propagated. It is also demonstrated that Airy beams can be exploited to carry orbital angular momentum (OAM) modes by applying an azimuthal spiral phase component to a circular Airy beam [20]. Moreover, by taking advantage of the nondiffracting feature of the Airy beam, enhancement of wireless power transmission efficiency is numerically validated [21]. These examples show that the Airy beam can be of significant interest in microwave applications, such as noncontact recognition, remote sensing, microwave detection, and radiofrequency identification.

*sburokur@parisnanterre.fr
†jianjia.yi@xjtu.edu.cn
‡zhangkuang@hit.edu.cn

 © 2020 American Physical Society

Metasurfaces, the two-dimensional version of metamaterials, have recently experienced rapid development due to their superior abilities to arbitrarily manipulate phase, amplitude, and polarization of electromagnetic (EM) waves. To date, various interesting functionalities are tailored from metasurfaces, including polarization conversion and control [22–25], holographic imaging [26–29], wave-front manipulation [30–46], vortex-beam generation [47–51], lenses [52–59], microwave antennas [60–66], mantle cloaking [67,68], and isolators [69]. Due to the flexibility in modulating EM waves, different Airy-beam generators are proposed based on the utilization of passive metasurfaces [70–75]. However, several applications, such as energy transfer or imaging, may demand control of the generated beam.

Here, we propose to use a programmable 1-bit coding metasurface that allows the Airy beam to be dynamically synthesized and manipulated by phase modulation of the incoming plane wave. The phase-coding profile for different Airy-beam parameters is realized by changing the voltage applied to the varactor diodes incorporated in the meta-atoms constituting the metasurface. The nondiffracting, self-bending, and self-healing properties of the Airy beam are first analyzed through different parameters characterizing such a waveform. In addition, frequency tuning of the Airy beam is achieved over a wide frequency band, spanning from 9 to 12 GHz. Furthermore, an additional linear phase profile is combined with the phase distribution of the Airy field envelope to steer the Airy beam to a desired direction. Both numerical simulations and experimental measurements are performed to validate the generation and dynamic manipulation of the Airy beam. Such flexible control of the propagation trajectory of an Airy beam can be potentially exploited in applications such as microwave imaging and wireless communication systems.

II. AIRY-BEAM GENERATION AND MANIPULATION MECHANISM

To analyze the propagation behavior of Airy beams, we consider the normalized paraxial equation of diffraction [2,3]:

$$i\frac{\partial\phi}{\partial\xi}+\frac{1}{2}\frac{\partial^2\phi}{\partial s^2}=0, \tag{1}$$

where ϕ is the electric field envelope. The parameter $s=by$ represents a dimensionless transverse coordinate (with b being an arbitrary transverse scale); $\xi=zb^2/k$ is the normalized propagation distance and $k=2\pi n/\lambda_0$ is the wave number (with λ_0 being the operating wavelength in free space). The electric field envelope of the Airy beam can be described as [2]:

$$\phi(\xi,s)=\mathrm{Ai}\left[s-\left(\frac{\xi}{2}\right)^2+i\alpha\xi\right]\exp\left[\alpha s-\left(\frac{\alpha\xi^2}{2}\right)-i\left(\frac{\xi^3}{12}\right)+i\left(\frac{\alpha^2\xi}{2}\right)+i\left(\frac{s\xi}{2}\right)\right], \tag{2}$$

where $\mathrm{Ai}(s)$ represents the Airy function. The decay factor α in the exponential truncation factor is a small positive value ($\alpha\ll1$) to ensure a containment of the infinite Airy tail, and therefore, a physical realization of such a beam. The initial field envelope of the finite Airy beam is then written as

$$\phi(\xi=0,y)=\mathrm{Ai}(by)\exp(ay), \tag{3}$$

with $a=\alpha b$.

Airy beams can be generated by modulating either amplitude and phase simultaneously or phase only along a metasurface. In the present work, the engineered metasurface allows control of only the phase, as schematically illustrated in Fig. 1. The phase modulation profile, which varies between $-\pi/2$ and $+\pi/2$, is represented by the blue line and is described as a function of the y coordinate as

$$\varphi=\arg[\phi(\xi=0,y)]-\frac{\pi}{2}. \tag{4}$$

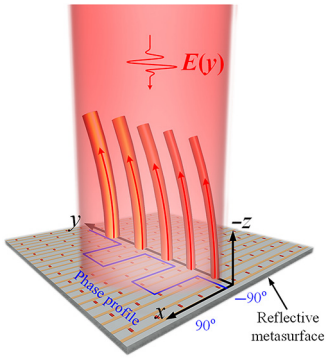

FIG. 1. Schematic illustration of Airy-beam generation when the proposed electronically programmable metasurface is illuminated by a y-polarized quasi-plane-wave emitted by a microwave horn antenna. Wave vector of the generated Airy beam is marked by red arrows, the direction of which is opposite to the incident quasi-plane-wave. Appropriate 1-bit coding phase distribution (blue line) is implemented by designing two distinct "0" and "1" control states as digital codes for $-\pi/2$ and $+\pi/2$ phase values, respectively.

III. DESIGN OF THE PROGRAMMABLE 1-BIT PHASE-CODING METASURFACE

An electronically programmable metasurface is exploited to generate and dynamically manipulate Airy beams.

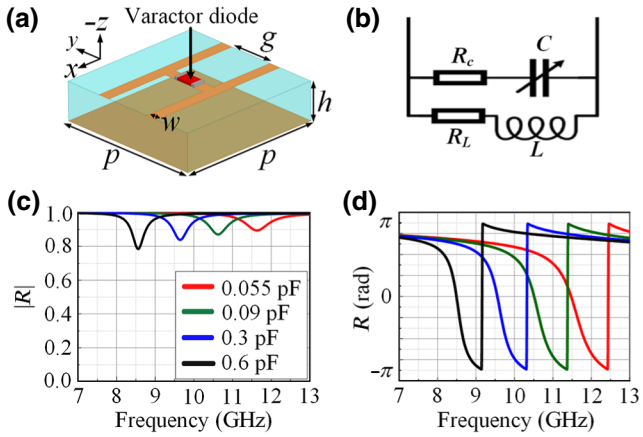

FIG. 2. (a) Schematic design of the elementary meta-atom consisting of two metallic strips printed on a grounded dielectric substrate. Geometrical dimensions are $w = 0.5$ mm, $g = 1.9$ mm, $p = 6$ mm, and $h = 1.52$ mm. Varactor diode is embedded in the gap between two metallic strips. (b) Equivalent *RLC* circuit of the meta-atom. (c),(d) Reflection magnitude and phase versus frequency of the meta-atom for different capacitance values of the varactor diode.

The elementary meta-atom, having a period of $p = 6$ mm, as shown in Fig. 2(a), is composed of two parallel metallic strips printed on the top surface of a low-loss grounded dielectric substrate ($\varepsilon_r = 4.5$ and $\tan\delta = 0.0035$) of thickness $h = 1.52$ mm. The two strips of width $w = 0.5$ mm are separated by a gap of $g = 1.9$ mm. The top layer, which is composed of the two microstrip lines, acts as a capacitive layer when the electric field is oriented perpendicular to the two lines. An inductive part is also created due to magnetic flux between the ground plane of the substrate (bottom layer) and the wire array (top layer).

While *p-i-n* diodes can offer only two different states (on and off), they are widely used in digital meta-atoms to achieve binary phase states [27,42]. Varactor diodes can provide a more flexible solution for realizing real-time reconfigurability, since the capacitance value can be modified continuously with a change in applied bias voltage. Therefore, to dynamically tune the response of the unit cell, a MACOM MGV 125-08 varactor diode is embedded in the gap between these two adjacent strips. The strips are further utilized as biasing lines for the varactor diodes, facilitating electronic control of the metasurface. The bottom face of the dielectric substrate is composed of a continuous metallic ground plane. To examine the behavior of the structure, the reflection properties of the meta-atom under periodic boundary conditions are calculated numerically with the finite-element method (FEM) Maxwell's equations solver of the high-frequency structure simulator (HFSS) commercial code by ANSYS.

In the numerical simulations, a uniform electromagnetic plane wave with the electric field oriented along the y axis is normally incident on the metasurface. Different capacitance values, varying from 0.055 to 0.6 pF, are applied according to the capacitance range of the varactor diode that will be implemented in the proof-of-concept prototype. The equivalent *RLC* circuit of the designed unit cell is shown in Fig. 2(b). The varactor diode's capacitance together with the inductive response of the structure results in an *LC* resonance of the meta-atom. To electronically tune the resonance frequency of the meta-atom, the separation, g, between the adjacent metallic strips is optimized such that the intrinsic capacitance of the unit cell can be ignored with respect to that of the varactor diode. Therefore, the only capacitance that influences the resonance frequency of the *RLC* circuit is the one from the varactor diode.

The simulated reflection magnitude and phase responses of the meta-atom are displayed in Figs. 2(c) and 2(d), respectively. As it can be clearly observed, the resonance frequency shifts from 8.4 to 11.6 GHz when the capacitance value is varied within the dynamic capacitance range of the varactor diode, and a phase variation close to 2π, together with a high reflection, can be obtained over a broad frequency range. As such, the two phase values of $-\pi/2$ and $+\pi/2$ required to generate the Airy beam can be achieved from the 1-bit phase-coding metasurface by changing the capacitance through the applied bias voltage. Although the proposed metasurface is designed for phase modulation only, the amplitude unintentionally changes slightly when the capacitance is modified, but with almost no effect on the generation of the Airy beam.

To highlight the properties of our proposed reconfigurable metasurface, a comparison with other metasurfaces using different techniques is made in Table I. The 28.6% frequency bandwidth clearly demonstrates the wideband property of our metasurface. In Ref. [42], a time-domain coding metasurface with a narrower frequency bandwidth

TABLE I. Comparison with recent studies on reconfigurable metasurface designs.

Ref.	Frequency bandwidth (GHz)	Experimental efficiency	Type	Electronic component	Modulation along metasurface
Zhang *et al.* [42]	9.2–10.2(10.3%)	Not given	Reflection	*p-i-n* diodes	Phase
Taravati and Eleftheriades [45]	5.28–5.33(0.9%)	Not given	Transmission	Varactor diodes	Phase
Taravati *et al.* [69]	5.8–6(3.4%)	Not given	Transmission	Transistor-based amplifiers	None
This work	9–12(28.6%)	32.4%	Reflection	Varactor diodes	Phase

of 10.3% that uses *p*-*i*-*n* diodes to control scattered far-field patterns is proposed. The structure allows arbitrary multibit programmable phases to be dynamically realized by manipulating the time-coding sequences of a physical 2-bit coding metasurface. Electronic components are also implemented in nonreciprocal metasurfaces [45,69]. The metasurface presented in Ref. [45] is composed of coupled time-modulated meta-atoms and can realize a nonreciprocal phase gradient on the two sides of the metasurface, such that the incoming (received) and outgoing (transmitted) waves are radiated at different radiation angles. In Ref. [69], the transistor-based amplifiers are implemented to achieve a spatial isolator with transmission gain in one direction and transmission loss in the other direction. However, these two nonreciprocal metasurfaces are subjected to the problem of a narrow frequency range.

IV. NUMERICAL AND EXPERIMENTAL VERIFICATIONS

A. Airy-beam generation

To validate the aforementioned Airy-beam generation, full-wave numerical simulations and experimental measurements are performed on the designed metasurface. The metasurface is illuminated by an incident plane wave in simulations (quasi-plane-wave from a microwave horn antenna in experiments) and is able to phase modulate the incident wave to reflect an Airy beam in the *y*-0-*z* plane. A prototype of the metasurface composed of 30×30 unit cells is fabricated by the printed circuit board technique and surface-mount component soldering. A photograph of the realized sample is shown in Fig. 3(a). An electronic control board connected to the metasurface is used to control the voltage applied to each column of 30 meta-atoms, and therefore, to adjust the capacitance in each column.

To experimentally measure the reflected electric field in the *y*-0-*z* plane, a measurement system in a microwave anechoic chamber is set up, as illustrated in Fig. 3(b). In this system, a 2–18 GHz wideband horn antenna placed at 1.5 m from the metasurface is used as a primary source to generate quasi-plane-waves. A fiber-optic active antenna used as a probe is mounted on two orthogonal linear computer-controlled translation stages to scan the electric field. The probe is stepped in small increments of 2 mm and is used to measure both the amplitude and phase of the electric field at each step, allowing a full two-dimensional electric field mapping to be performed over a maximum scanning area of 400×400 mm^2 in the *y*-0-*z* plane. Both the horn antenna and the probe are connected to the two ports of an Agilent 8722ES network analyzer.

First, we start by generating different Airy beams at 10 GHz. The wave packet of the Airy beam is appropriately designed with an initial field envelope of the finite Airy beam calculated from Eq. (3). ϕ oscillates around zero along the *y* axis with the exponential decaying amplitude. Parameter *a* influences only the amplitude of the Airy beam due to its presence in the exponential term $\exp(ay)$. No matter how parameter *a* changes, the zero position of ϕ is kept fixed. Here, the Airy beam is generated using phase modulation only. When ϕ is positive, the phase is set as $-\pi/2$ and, for negative values of ϕ, the phase is set to $+\pi/2$. The phase varies with the change of the zero position of ϕ.

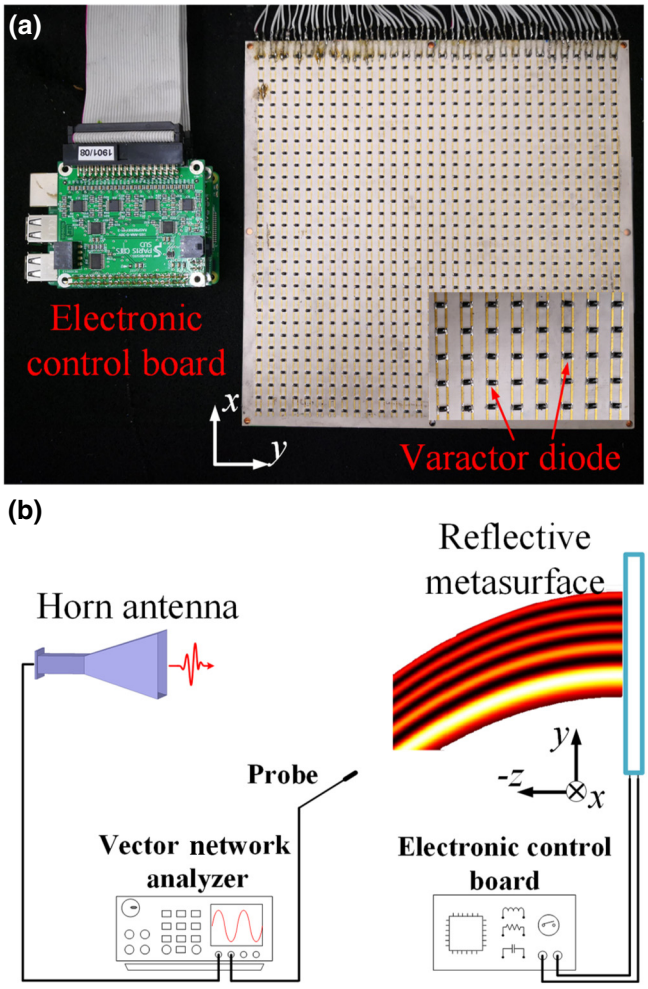

FIG. 3. (a) Photograph of the fabricated prototype and electronic control board. Inset shows the varactor diodes soldered on the metasurface. (b) Schematic illustration of the experimental measurement setup used to scan the electric field distribution.

To analyze the influence of the transverse coordinate on the parabolic trajectory of the main beam, four configurations of Airy function parameters $(a, b) = (4, 44.1)$, $(4, 50)$, $(4, 55.7)$, and $(4, 61)$ are applied to the metasurface through the corresponding capacitance values (in simulations) and bias voltages (in experiments), as presented in Fig. 4(a). In all configurations, $a = 4$ and the parameter *b* is varied. By fixing parameter *a*, the exponential truncation factor is kept

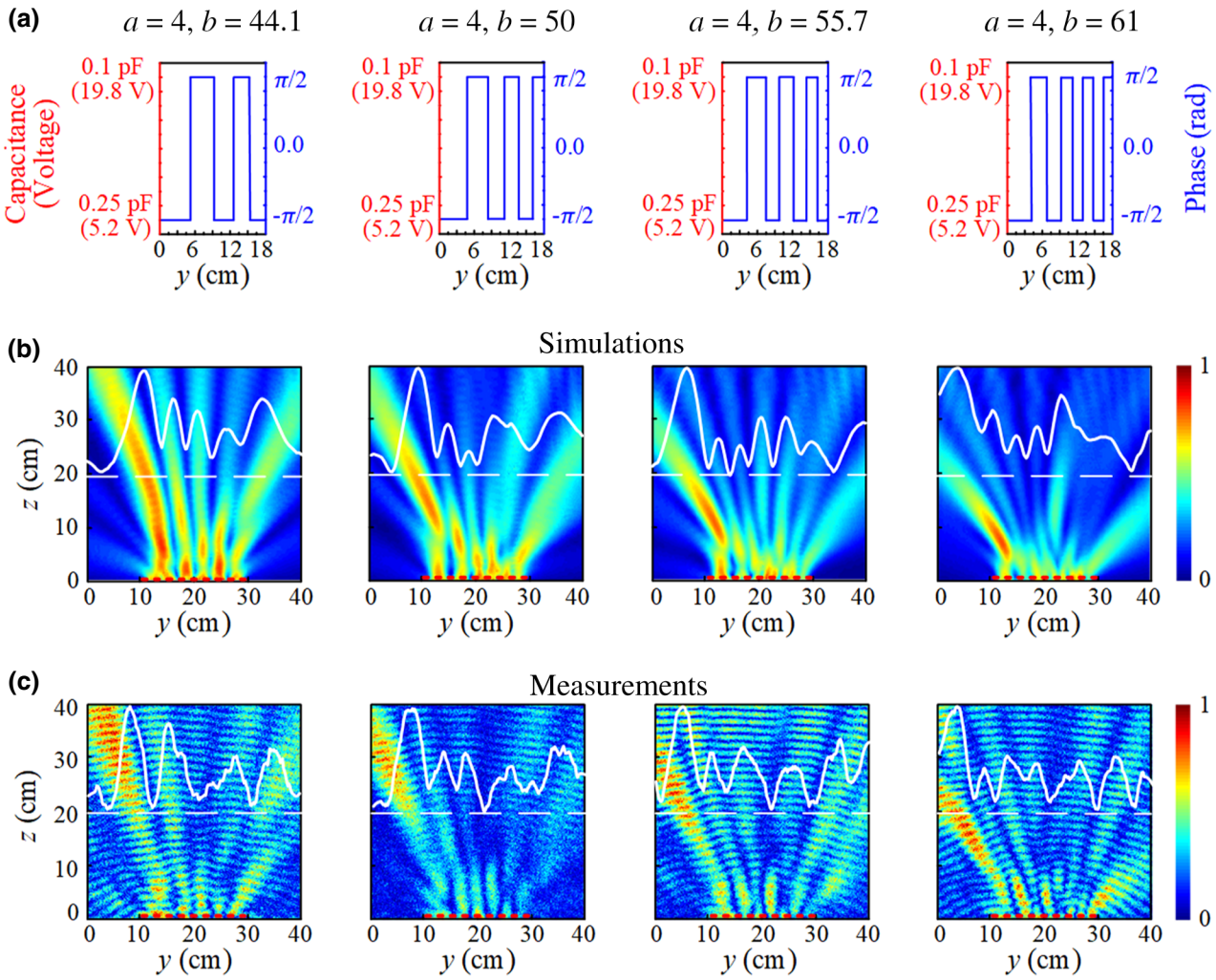

FIG. 4. Airy-beam generation using different parameters at 10 GHz. (a) Phase profile for four Airy function sets of parameters $a = 4$ and $b = 44.1$ (5 sections), $a = 4$ and $b = 50$ (6 sections), $a = 4$ and $b = 55.7$ (7 sections), and $a = 4$ and $b = 61$ (8 sections). Capacitance and voltage values applied to achieve the two digital states "0" and "1" (phase values of $-\pi/2$ and $+\pi/2$, respectively) are shown. (b) Electric field distribution in the y-0-z plane obtained from numerical simulations. Normalized amplitude (white line) of the Airy beam is displayed 20 cm away from the metasurface. (c) Experimentally measured electric field distribution in the y-0-z plane.

the same in all configurations. Parameter b presented in Eq. (3) allows the curvature of the Airy beam to be changed.

Both numerical and experimental electric field distributions of the generated Airy beam are presented in Figs. 4(b) and 4(c) for the different parameters. The results show clearly that an Airy beam is indeed generated by applying different calculated phase profiles. As the value of parameter b increases, the degree of curvature of the main beam also increases. The transverse offset of main lobe of the Airy beam increases for a fixed parameter b when the propagating distance increases. It is important to point out that Airy beams are inherently subjected to the paraxial limitation. As such, when a self-bending Airy beam moves along a parabolic trajectory and eventually bends into a large angle, it leaves its domain of existence and finally diffracts. The maximum angle for the paraxial approximation is generally taken as 10° [76,77]. The position of 10° between the wave vector of the main lobe of the Airy beam for parameter $b = 44.1$ and the z axis is located at around $z = 20$ cm. The main Airy lobe then starts to diffract at around $z = 26$ cm, which is further illustrated in Fig. 5(b). However, for parameter $b = 61$, the main Airy lobe reaches the paraxial approximation limit at around $z = 10$ cm. In such a configuration, the main beam maintains the diffraction-free property for a short distance and diffracts at around $z = 13$ cm.

The normalized amplitude (white line) of the Airy beam at 20 cm away from the metasurface is plotted in Figs. 4(b) and 4(c), where an exponential decaying feature can be observed together with a main beam. Due to the larger

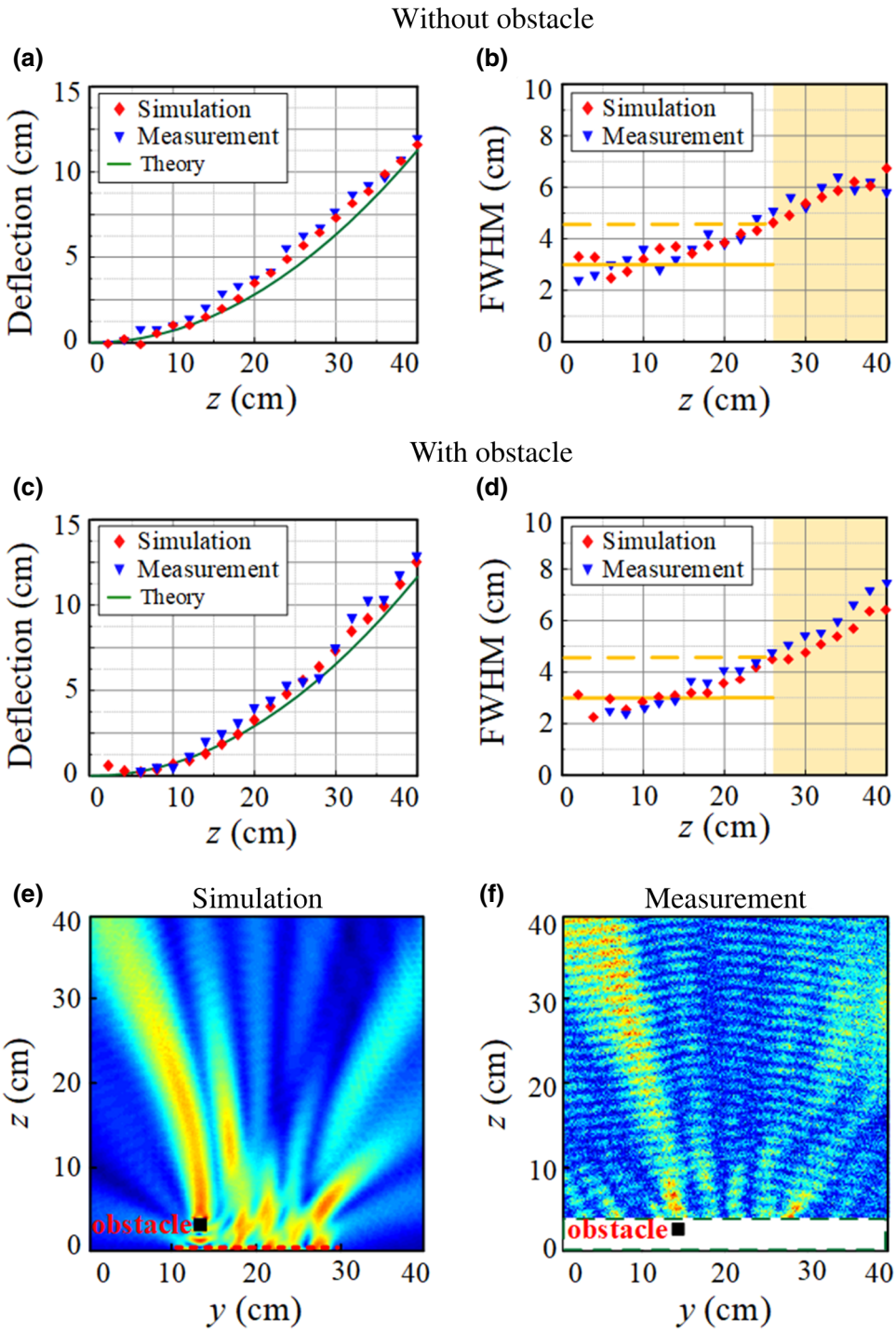

FIG. 5. Validation of the nondiffracting, self-bending, and self-healing properties of the Airy beam generated at 10 GHz for the configuration $a = 4$, $b = 44.1$. (a) Self-bending property of the Airy beam. Deflection of the main beam versus propagation distance (z direction) calculated from theory, simulation, and measurement. (b) Diffraction-free property of the Airy beam. Variation of FWHM of the main lobe along the z direction. Nondiffracting region is defined as the zone below the dotted yellow line, the value of which is 1.5 times the average FWHM value (solid yellow line) of the initial main beam where oscillatory patterns are observed. Yellow shaded zone represents the diffraction region. (c),(d) Deflection and FWHM results of main beam of the Airy beam with an obstacle (copper square barrier of $\lambda_0/2 \times \lambda_0/2$) located in the propagation path of main lobe. (e),(f) Self-healing property of the Airy beam validated numerically and experimentally in a complex environment comprising the presence of an obstacle.

number of $[-\pi/2, +\pi/2]$ oscillations when b increases, less interference of the side lobes with the Airy main lobe can be observed.

The self-bending characteristic of the Airy beam is investigated using the deflection offset of the main lobe with the transverse scale parameter $b = 44.1$ [Fig. 5(a)]. The deflection offset is calculated by the difference between the center position of the main beam in the Airy profile and that of a hypothetical beam propagating along a straight direction. Under the paraxial approximation, the deflection offset can be theoretically described as [3]

$$y_d \cong \lambda_0^2 z^2/(16\pi^2 {y_0}^3), \tag{5}$$

where $y_0 = 1/b \approx 22.7$ mm. The theoretically calculated deflection [green solid line in Fig. 5(a)] shows a smooth parabolic trajectory. The deflection of the Airy main lobe extracted from numerical simulations and experimental measurements are represented by the red and blue markers, respectively. The results indicate a good qualitative agreement between simulations, measurements, and theoretical predictions.

The full width at half maximum (FWHM) of the Airy main lobe as a function of the propagation distance is calculated to evaluate the diffraction-free property of the generated Airy beam [Fig. 5(b)]. Although a slightly oscillatory pattern around FWHM = 3 cm is exhibited at the initial stage of propagation, the nondiffraction property is clearly apparent in both simulations and measurements. The Airy beam generally diffracts beyond 1.5 times the average FWHM value of the initial main beam [72]. The average FWHM value is 3 cm, so the diffraction-free region will be located in the region where the FWHM is below 4.5 cm. The reason for the limited propagating distance within which the beam preserves its nondiffraction nature is that the Airy-beam packet is truncated to enable its physical realization. Additionally, the deflection and FWHM of the Airy main lobe are also plotted when a metallic obstacle is placed in its propagation path [Figs. 5(c) and 5(d), respectively]. In our case, the obstacle is a copper-based square barrier with geometrical dimensions of $15 \times 15\,\text{mm}^2$ ($\lambda_0/2 \times \lambda_0/2$). The obstacle is positioned at $(y, z) = (124.5\text{ mm}, 26\text{ mm})$, which is in the propagation path of the Airy main lobe.

When compared with the results obtained without the obstacle in Figs. 5(a) and 5(b), good agreement can be observed, which means the Airy beam recovers well after passing thorough the metallic obstacle. Moreover, the self-healing property of the Airy beam is validated both numerically and experimentally by displaying the electric field distribution in the y-0-z plane in the presence of the metallic obstacle in the propagation path of the main lobe, as shown in Figs. 5(e) and 5(f). The results show that the Airy beam is scattered locally by the square obstacle, but, even in such a complex environment with an obstacle, the evolution of the electric field arising from the self-healing property allows the Airy beam to recover rapidly, while maintaining its nondiffraction property.

B. Frequency agility

It is worth noting that the Airy-beam generator based on the electronically programmable metasurface can operate over a broad frequency band, ranging from 9 to 12 GHz. To realize the frequency-agility mechanism, the phase profiles at different frequencies are calculated and shown in Fig. 6(a). Using the appropriate phase profiles, numerical simulations and experimental measurements are performed and the results are displayed in Figs. 6(b) and 6(c). The numerical and experimental electric field distributions share the same Airy function parameters, $a = 4$ and $b = 44.1$. Moreover, as depicted in Fig. 6(d), the deflection offset in the y direction of the main lobe decreases slightly with an increase in frequency and good qualitative agreement can be observed between theory, numerical simulations, and experimental measurements. As illustrated in Fig. 6(e), the diffraction-free regions for different frequencies are almost the same, which suggests that the Airy beam is well generated by the metasurface over a wide frequency band.

To quantitatively evaluate the performances of the 1-bit phase-coding programmable metasurface as an Airy-beam generator, the total efficiency, η_{total}, is calculated as

$$\eta_{\text{total}} = \frac{P_{\text{Airy}}}{P_{\text{inc}}}, \tag{6}$$

where P_{Airy} is the power carried by the reflected Airy beam (comprising the Airy main lobe and the side lobes) and P_{inc} is the power associated with the incident wave. For Airy function parameters $a = 4$ and $b = 44.1$ over the 9 to 12 GHz frequency band, the simulated and measured efficiency is, on average, 36.4% and 32.4%, respectively. Additionally, the efficiency of the Airy main lobe, defined by the ratio of the power carried by the Airy main lobe divided by the power carried by the Airy beam (main and side lobes), approaches 45% in both simulations and measurements.

Due to the resonant nature of the elementary cell and ohmic losses caused by the inclusion of varactor diodes, the reflection amplitude varies slightly when the capacitance is changed. To illustrate the influence of the inhomogeneous reflection amplitude on the efficiency, different dielectric losses ($\tan\delta$) of the substrate are considered in simulations. The simulated efficiencies are investigated at 10 GHz and are calculated to be 38.61%, 37.69%, and 30.75% for $\tan\delta = 0.0035$, 0.007, and 0.021, respectively. These results suggest that the inhomogeneous reflection amplitude along the metasurface can lead to a drop in efficiency.

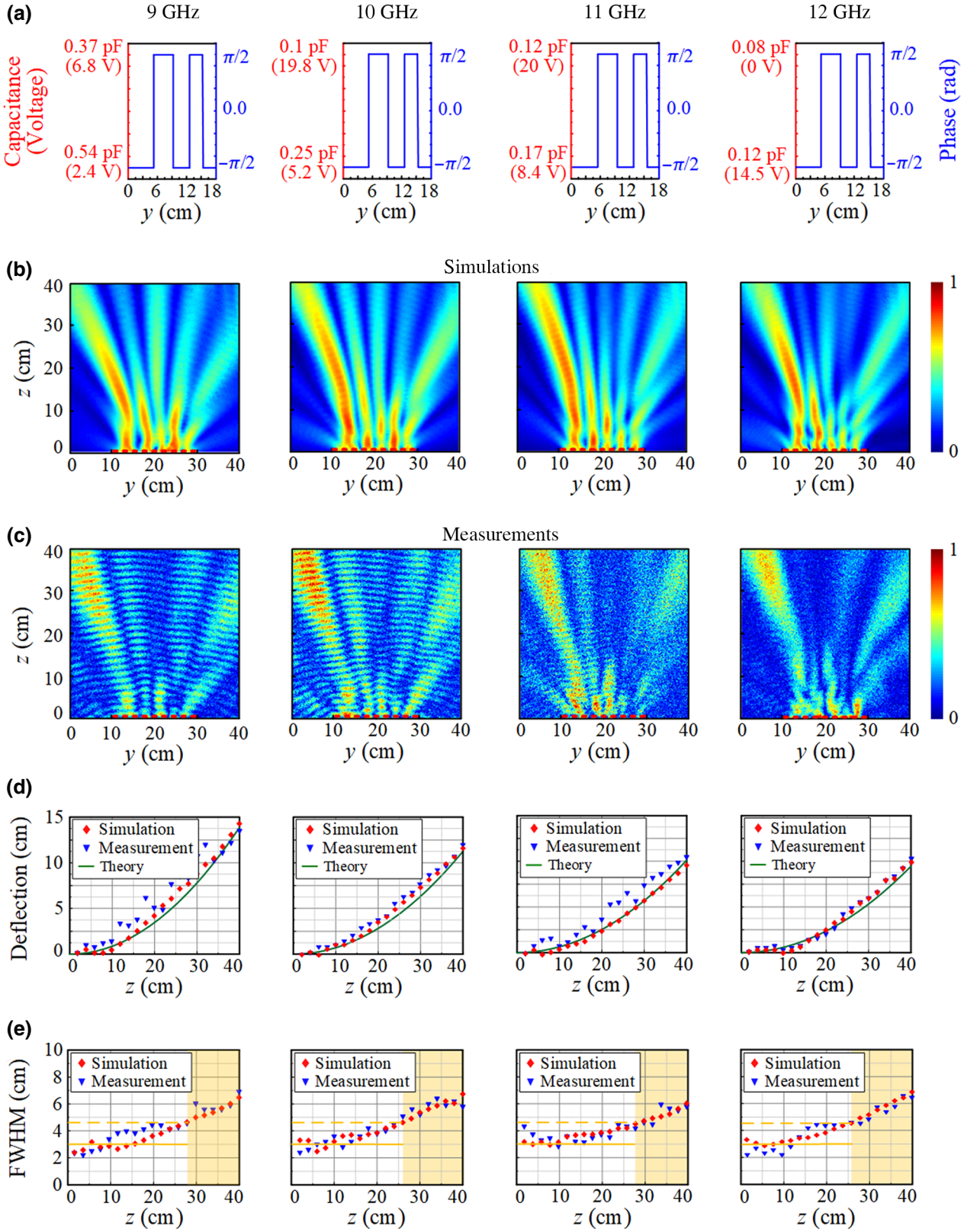

FIG. 6. (a) Phase profiles for Airy function parameters $a = 4$ and $b = 44.1$ at different frequencies. (b),(c) Electric field distribution obtained from numerical simulations and experimental measurements. (d) Deflection of the Airy main lobe versus propagation distance (z direction) extracted from theory, simulation, and measurement. (e) Variation of FWHM of the Airy main lobe along the z direction for both simulations and measurements. Yellow shaded zone represents the diffraction region.

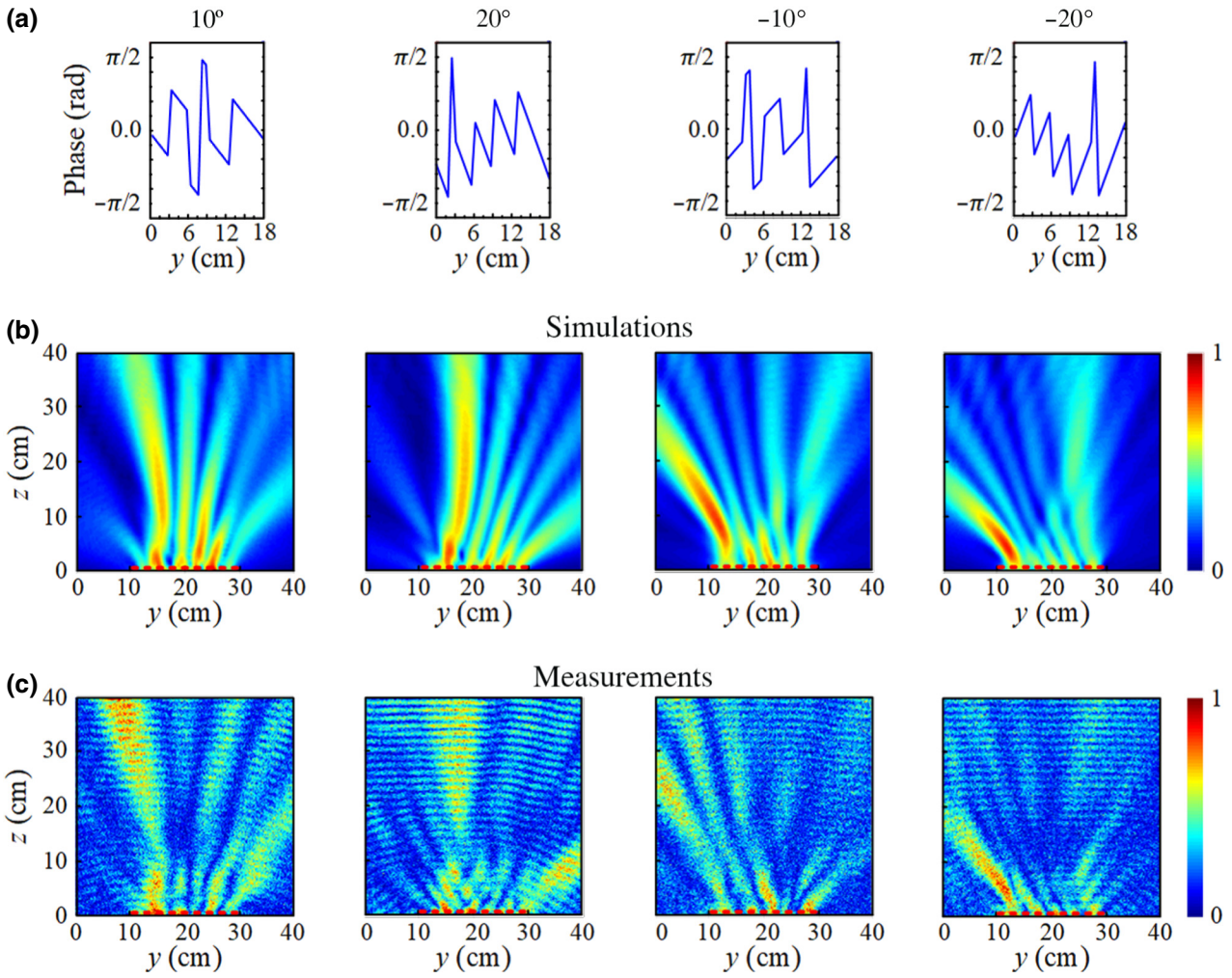

FIG. 7. Beam steering of the Airy beam for $a = 4$ and $b = 44.1$ at 10 GHz. (a) Phase profiles calculated from Eq. (8) and implemented on the metasurface. (b),(c) Electric field distribution obtained from numerical simulations and experimental measurements for different deflection angles (−10°, 10°, −20°, and 20°).

C. Steering of the Airy beam

To illustrate the flexibility provided by our reconfigurable metasurface in manipulating the Airy beam, the direction control of the Airy main lobe is investigated by combining an additional linear phase profile to the Airy-beam phase profile. According to the generalized Snell law, when an incident wave illuminates a reflective metasurface, the direction of the reflected wave depends on the phase gradient applied to the metasurface [30]:

$$k_0 \sin\theta_r - k_0 \sin\theta_i = \frac{d\psi}{dy}, \tag{7}$$

where θ_i and θ_r represent the angles of incident and reflected waves, respectively;k_0 is the propagation constant in free space; and $d\psi/dy$ is the phase gradient applied to the metasurface. Here, we fix the incidence angle to 0°. Thus, the phase profile for an Airy beam with a desired deflection angle, θ_{def}, is described as

$$\theta_{\text{def}} = \arg[\phi(\xi = 0, y)] - \frac{\pi}{2} + y k_0 \sin\theta_{\text{def}}. \tag{8}$$

The phase profiles for four different deflection angles (−20°, −10°, 10°, and 20°) are calculated for the configuration with Airy function parameters $a = 4$ and $b = 44.1$. As depicted in Fig. 7, the Airy beam, including the main lobe and all side lobes, is deflected to the predefined radiation direction angle with respect to the original position. The main beam and exponential decaying feature for both simulation and measurement can be clearly observed. The experimental results are in good agreement with the simulated ones. These results suggest the possibility of flexibly manipulating the Airy beam with respect to the local application environment, particularly for microwave communication and detection systems.

V. CONCLUSION

In summary, dynamic generation and manipulation of an Airy beam are demonstrated by exploiting a 1-bit phase-coding programmable metasurface at microwave frequencies. The metasurface first allows different Airy beams with different sets of Airy function parameters to be generated and controlled. The nondiffracting, self-bending, and self-healing properties of the generated Airy beams are validated numerically and experimentally. Furthermore, the frequency-agility mechanism is demonstrated over a wide frequency band, spanning from 9 to 12 GHz. Finally, a step further is made in the manipulation of Airy beams. Taking advantage of the flexibility provided by the programmable metasurface, we experimentally show that the radiation direction of the Airy beam can be controlled by combining the Airy phase profile with an additional linear phase profile.

With appropriate fabrication technology and reconfigurability mechanism, the design principle can be extended to millimeter-wave, terahertz, and optical frequencies for potential applications in micromachining, medical lasers, optical trapping and manipulation, and imaging.

ACKNOWLEDGMENTS

This work is awarded the Doctoral Students' Long-Term Study Abroad Scholarship Fund of Xidian University and is supported by the Chinese Scholarship Council.

[1] M. Berry and N. Balazs, Nonspreading wave packets, Am. J. Phys. **47**, 264 (1979).
[2] G. A. Siviloglou and D. N. Christodoulides, Accelerating finite energy Airy beams, Opt. Lett. **32**, 979 (2007).
[3] G. A. Siviloglou, J. Broky, A. Dogariu, and D. N. Christodoulides, Observation of Accelerating Airy Beams, Phys. Rev. Lett. **99**, 213901 (2007).
[4] J. Baumgartl, M. Mazilu, and K. Dholakia, Optically mediated particle clearing using Airy wavepackets, Nat. Photonics **2**, 675 (2008).
[5] H. Cheng, W. Zang, W. Zhou, and J. Tian, Analysis of optical trapping and propulsion of Rayleigh particles using Airy beam, Opt. Express **18**, 20384 (2010).
[6] P. Zhang, J. Prakash, Z. Zhang, M. S. Mills, N. K. Efremidis, D. N. Christodoulides, and Z. G. Chen, Trapping and guiding microparticles with morphing autofocusing Airy beams, Opt. Lett. **36**, 2883 (2011).
[7] Z. Zhao, W. Zang, and J. Tian, Optical trapping and manipulation of Mie particles with Airy beam, J. Opt. **18**, 025607 (2016).
[8] B. K. Singh, H. Nagar, Y. Roichman, and A. Arie, Particle manipulation beyond the diffraction limit using structured super-oscillating light beams, Light: Sci. Appl. **6**, e17050 (2017).
[9] BŞ Călin, L. Preda, F. Jipa, and M. Zamfirescu, Laser fabrication of diffractive optical elements based on detour-phase computer-generated holograms for two-dimensional Airy beams, Appl. Opt. **57**, 1367 (2018).
[10] M. Manousidaki, V. Y. Fedorov, D. G. Papazoglou, M. Farsari, and S. Tzortzakis, in Proc. SPIE 11168, Advanced Manufacturing Technologies for Micro- and Nanosystems in Security and Defence II (2019), pp. 1116802.
[11] D. Abdollahpour, S. Suntsov, D. G. Papazoglou, and S. Tzortzakis, Spatiotemporal Airy Light Bullets in the Linear and Nonlinear Regimes, Phys. Rev. Lett. **105**, 253901 (2010).
[12] D. Bongiovanni, B. Wetzel, Y. Hu, Z. Chen, and R. Morandotti, Optimal compression and energy confinement of optical Airy bullets, Opt. Express **24**, 26454 (2016).
[13] Y. Peng, B. Chen, X. Peng, M. Zhou, L. Zhang, D. Li, and D. Deng, Self-accelerating Airy-ince-Gaussian and Airy-helical-ince-Gaussian light bullets in free space, Opt. Express **24**, 18973 (2016).
[14] Z. Wu, Z. Wang, H. Guo, W. Wang, and Y. Gu, Self-accelerating Airy-laguerre-Gaussian light bullets in a two-dimensional strongly nonlocal nonlinear medium, Opt. Express **25**, 30468 (2017).
[15] S. Jia, J. C. Vaughan, and X. Zhuang, Isotropic three-dimensional super-resolution imaging with a self-bending point spread function, Nat. Photonics **8**, 302 (2014).
[16] T. Vettenburg, H. I. C. Dalgarno, J. Nylk, C. Coll-Llado, D. E. K. Ferrier, T. Cizmar, F. J. Gunn-Moore, and K. Dholakia, Light-sheet microscopy using an Airy beam, Nat. Methods **11**, 541 (2014).
[17] H. He, C. Kong, X. Tan, K. Y. Chan, Y. Ren, K. K. Tsia, and K. K. Y. Wong, Depth-resolved volumetric two-photon microscopy based on dual Airy beam scanning, Opt. Lett. **44**, 5238 (2019).
[18] X. Tan, C. Kong, Y. Ren, C. S. W. Lai, K. K. Tsia, and K. K. Y. Wong, Volumetric two-photon microscopy with a non-diffracting Airy beam, Opt. Lett. **44**, 391 (2019).
[19] I. D. Chremmos, G. Fikioris, and N. K. Efremidis, Accelerating and abruptly-autofocusing beam waves in the fresnel zone of antenna arrays, IEEE Trans. Antennas Propag **61**, 5048 (2013).
[20] R. Kadlimatti and P. V. Parimi, Millimeter-wave non-diffracting circular Airy OAM beams, IEEE Trans. Antennas Propag **67**, 260 (2018).
[21] Z. Yang, G. Wen, D. Inserra, and Y. Huang, in 2018 IEEE MTT-S International Wireless Symposium (IWS), Chengdu, (2018), pp. 1–3.
[22] D. Wang, Y. Gu, Y. Gong, C.-W. Qiu, and M. Hong, An ultrathin terahertz quarter-wave plate using planar babinet-inverted metasurface, Opt. Express **23**, 11114 (2015).
[23] J. D. Baena, J. P. Del Risco, A. P. Slobozhanyuk, S. B. Glybovski, and P. A. Belov, Self-complementary metasurfaces for linear-to-circular polarization conversion, Phys. Rev. B **92**, 245413 (2015).
[24] B. Ratni, A. de Lustrac, G.-P. Piau, and S. N. Burokur, Electronic control of linear-to-circular polarization conversion using a reconfigurable metasurface, Appl. Phys. Lett. **111**, 214101 (2017).
[25] Z. Wu, Y. Ra'di, and A. Grbic, Tunable Metasurfaces: A Polarization Rotator Design, Phys. Rev. X **9**, 011036 (2019).
[26] D. Wen, F. Yue, G. Li, G. Zheng, K. Chan, S. Chen, M. Chen, K. F. Li, P. W. H. Wong, K. W. Cheah, E. Y. B. Pun,

S. Zhang, and X. Chen, Helicity multiplexed broadband metasurface holograms, Nat. Commun. **6**, 8241 (2015).
[27] L. Li, T. J. Cui, W. Ji, S. Liu, J. Ding, X. Wan, Y. B. Li, M. Jiang, C.-W. Qiu, and S. Zhang, Electromagnetic reprogrammable coding-metasurface holograms, Nat. Commun. **8**, 197 (2017).
[28] Z. Wang, X. Ding, K. Zhang, B. Ratni, S. N. Burokur, X. Gu, and Q. Wu, Huygens metasurface holograms with the modulation of focal energy distribution, Adv. Opt. Mater. **6**, 1800121 (2018).
[29] Z. Wang, J. Liu, X. Ding, W. Zhao, K. Zhang, H. Li, B. Ratni, S. N. Burokur, and Q. Wu, Three-dimensional microwave holography based on broadband huygens' metasurface, Phys. Rev. Appl **13**, 014033 (2020).
[30] N. Yu, P. Genevet, M. A. Kats, F. Aieta, J.-P. Tetienne, F. Capasso, and Z. Gaburro, Light propagation with phase discontinuities: Generalized laws of reflection and refraction, Science **334**, 333 (2011).
[31] N. M. Estakhri and A. Alù, Wave-Front Transformation With Gradient Metasurfaces, Phys. Rev. X **6**, 041008 (2016).
[32] A. Epstein and G. V. Eleftheriades, Huygens' metasurfaces via the equivalence principle: Design and applications, J. Opt. Soc. Am. B **33**, A31 (2016).
[33] Y. Ra'di, D. L. Sounas, and A. Alù, Metagratings: Beyond the Limits of Graded Metasurfaces for Wave Front Control, Phys. Rev. Lett. **119**, 067404 (2017).
[34] A. Epstein and O. Rabinovich, Unveiling the Properties of Metagratings via a Detailed Analytical Model for Synthesis and Analysis, Phys. Rev. Appl. **8**, 054037 (2017).
[35] A. Díaz-Rubio, V. S. Asadchy, A. Elsakka, and S. A. Tretyakov, From the generalized reflection law to the realization of perfect anomalous reflectors, Sci. Adv. **3**, e1602714 (2017).
[36] B. Ratni, A. de Lustrac, G.-P. Piau, and S. N. Burokur, Reconfigurable meta-mirror for wavefronts control: Applications to microwave antennas, Opt. Express **26**, 2613 (2018).
[37] V. Popov, F. Boust, and S. N. Burokur, Controlling Diffraction Patterns with Metagratings, Phys. Rev. Appl. **10**, 011002 (2018).
[38] Y. Yuan, K. Zhang, X. Ding, B. Ratni, S. N. Burokur, and Q. Wu, Complementary transmissive ultra-thin metadeflectors for broadband polarization-independent refractions in the microwave region, Photonics Res. **7**, 80 (2019).
[39] V. Popov, F. Boust, and S. N. Burokur, Constructing the Near Field and far Field with Reactive Metagratings: Study on the Degrees of Freedom, Phys. Rev. Appl. **11**, 024074 (2019).
[40] O. Rabinovich and A. Epstein, Arbitrary diffraction engineering with multilayered multielement metagratings, IEEE Trans. Antennas Propag. **68**, 1553 (2020).
[41] V. Popov, F. Boust, and S. N. Burokur, Beamforming with metagratings at microwave frequencies: Design procedure and experimental demonstration, IEEE Trans. Antennas Propag. **68**, 1533 (2020).
[42] L. Zhang, Z. X. Wang, R. W. Shao, J. L. Shen, X. Q. Chen, X. Wan, Q. Cheng, and T. J. Cui, Dynamically realizing arbitrary multi-bit programmable phases using a 2-bit time-domain coding metasurface, IEEE Trans. Antennas Propag. **68**, 2984 (2020).
[43] R. Wu, L. Bao, L. Wu, and T. Cui, Broadband transmission-type 1-bit coding metasurface for electromagnetic beam forming and scanning, Sci. China Phys. Mech. **63**, 284211 (2020).
[44] L. Bao, R. Y. Wu, X. Fu, Q. Ma, G. D. Bai, J. Mu, R. Jiang, and T. J. Cui, Multi-beam forming and controls by metasurface with phase and amplitude modulations, IEEE Trans. Antennas Propag. **67**, 6680 (2019).
[45] S. Taravati and G. V. Eleftheriades, Full-duplex nonreciprocal-beam-steering metasurfaces comprising time-modulated twin meta-atoms, arXiv:1911.04033v1 [physics.app-ph] (2019).
[46] S. Taravati and G. V. Eleftheriades, Generalized Space-Time-Periodic Diffraction Gratings: Theory and Applications, Phys. Rev. Appl. **12**, 024026 (2019).
[47] S. Yu, L. Li, G. Shi, C. Zhu, X. Zhou, and Y. Shi, Design, fabrication, and measurement of reflective metasurface for orbital angular momentum vortex wave in radio frequency domain, Appl. Phys. Lett. **108**, 121903 (2016).
[48] S. Yu, L. Li, G. Shi, C. Zhu, and Y. Shi, Generating multiple orbital angular momentum vortex beams using a metasurface in radio frequency domain, Appl. Phys. Lett. **108**, 241901 (2016).
[49] J. Zeng, L. Li, X. Yang, and J. Gao, Generating and separating twisted light by gradient–rotation split-ring antenna metasurfaces, Nano Lett. **16**, 3101 (2016).
[50] K. Zhang, Y. Yuan, X. Ding, B. Ratni, S. N. Burokur, and Q. Wu, High efficiency metalenses with switchable functionalities in microwave region, ACS. Appl. Mater. Interfaces **11**, 28423 (2019).
[51] K. Zhang, Y. Wang, Y. Yuan, and S. N. Burokur, A review of orbital angular momentum vortex beams generation: From traditional methods to metasurfaces, Appl. Sci. **10**, 10031015 (2020).
[52] A. Dhouibi, S. N. Burokur, A. de Lustrac, and A. Priou, Metamaterial-based half Maxwell fish-eye lens for broadband directive emissions, Appl. Phys. Lett. **102**, 024102 (2013).
[53] C. Pfeiffer and A. Grbic, Metamaterial Huygens' Surfaces: Tailoring Wave Fronts with Reflectionless Sheets, Phys. Rev. Lett. **110**, 197401 (2013).
[54] N. Yu and F. Capasso, Flat optics with designer metasurfaces, Nat. Mater. **13**, 139 (2014).
[55] F. Monticone, N. M. Estakhri, and A. Alù, Full Control of Nanoscale Optical Transmission with a Composite Metascreen, Phys. Rev. Lett. **110**, 203903 (2013).
[56] X. Ding, F. Monticone, K. Zhang, L. Zhang, D. Gao, S. N. Burokur, A. de Lustrac, Q. Wu, C.-W. Qiu, and A. Alù, Ultrathin pancharatnam–berry metasurface with maximal cross-polarization efficiency, Adv. Mater. **27**, 1195 (2015).
[57] M. Veysi, C. Guclu, O. Boyraz, and F. Capolino, Reflective metasurface lens with an elongated needle-shaped focus, J. Opt. Soc. Am. B **34**, 374 (2017).
[58] K. Chen, Y. Feng, F. Monticone, J. Zhao, B. Zhu, T. Jiang, L. Zhang, Y. Kim, X. Ding, S. Zhang, A. Alù, and C. Qiu, A reconfigurable active huygens' metalens, Adv. Mater. **29**, 1606422 (2017).
[59] B. Ratni, Z. Wang, K. Zhang, X. Ding, A. de Lustrac, G.-P. Piau, and S. N. Burokur, Dynamically Controlling Spatial Energy Distribution with a Holographic Metamirror for Adaptive Focusing, Phys. Rev. Appl. **13**, 034006 (2020).

[60] S. N. Burokur, J.-P. Daniel, P. Ratajczak, and A. de Lustrac, Tunable bi-layered metasurface for frequency reconfigurable directive emissions, Appl. Phys. Lett. **97**, 064101 (2010).

[61] C. Pfeiffer, A. Grbic, and A. printed, Broadband luneburg lens antenna, IEEE Trans. Antennas Propag. **58**, 3055 (2010).

[62] A. Dhouibi, S. N. Burokur, A. de Lustrac, and A. Priou, Low-profile substrate-integrated lens antenna using metamaterials, IEEE Antennas Wireless Propag. Lett. **12**, 43 (2013).

[63] C. Pfeiffer and A. Grbic, Controlling Vector Bessel Beams with Metasurfaces, Phys. Rev. Appl. **2**, 044012 (2014).

[64] G. Minatti, M. Faenzi, E. Martini, F. Caminita, P. De Vita, D. Gonzalez-Ovejero, M. Sabbadini, and S. Maci, Modulated metasurface antennas for space: Synthesis, analysis and realizations, IEEE Trans. Antennas Propag **63**, 1288 (2015).

[65] A. Epstein, J. P. S. Wong, and G. V. Eleftheriades, Cavity-excited huygens' metasurface antennas for near-unity aperture illumination efficiency from arbitrarily large apertures, Nat. Commun. **7**, 10360 (2016).

[66] M. F. Imani, J. N. Gollub, O. Yurduseven, A. V. Diebold, M. Boyarsky, T. Fromenteze, L. Pulido-Mancera, T. Sleasman, and D. R. Smith, Review of metasurface antennas for computational microwave imaging, IEEE Trans. Antennas Propag. **68**, 1860 (2020).

[67] J. C. Soric, A. Monti, A. Toscano, F. Bilotti, and A. Alù, Dual-polarized reduction of dipole antenna blockage using mantle cloaks, IEEE Trans. Antennas Propag. **63**, 4827 (2015).

[68] T. V. Teperik, S. N. Burokur, A. de Lustrac, G. Sabanowski, and G.-P. Piau, Experimental validation of an ultra-thin metasurface cloak for hiding a metallic obstacle from an antenna radiation at low frequencies, Appl. Phys. Lett. **111**, 054105 (2017).

[69] S. Taravati, B. A. Khan, S. Gupta, K. Achouri, and C. Caloz, Nonreciprocal nongyrotropic magnetless metasurface, IEEE Trans. Antennas Propag. **65**, 3589 (2017).

[70] E. Song, G. Lee, H. Park, K. Lee, J. Kim, J. Hong, H. Kim, and B. Lee, Compact generation of Airy beams with C-aperture metasurface, Adv. Opt. Mater. **5**, 1601028 (2017).

[71] Q. Fan, D. Wang, P. Huo, Z. Zhang, Y. Liang, and T. Xu, Autofocusing Airy beams generated by all-dielectric metasurface for visible light, Opt. Express **25**, 9285 (2017).

[72] H. Li, W. Hao, X. Yin, S. Chen, and L. Chen, Broadband generation of Airy beams with hyperbolic metamaterials, Adv. Opt. Mater. **7**, 1900493 (2019).

[73] W. Hao, M. Deng, S. Chen, and L. Chen, High-efficiency Generation of Airy Beams with Huygens' Metasurface, Phys. Rev. Appl. **11**, 054012 (2019).

[74] H.-X. Xu, G. Hu, L. Han, M. Jiang, Y. Huang, Y. Li, X. Yang, X. Ling, L. Chen, J. Zhao, and C.-W. Qiu, Chirality-assisted high-efficiency metasurfaces with independent control of phase, amplitude, and polarization, Adv. Opt. Mater. **7**, 1801479 (2019).

[75] Z. Miao, Z. Hao, B. Jin, and Z. Chen, Low-profile two-dimensional THz Airy beam generator using the phase-only reflective metasurface, IEEE Trans. Antennas Propag. **68**, 1503 (2020).

[76] A. Wu, G. Kang, J. Zang, Y. Liu, X. Tan, T. Shimura, and K. Kuroda, Null reconstruction of orthogonal circular polarization hologram with large recording angle, Opt. Express **23**, 8880 (2015).

[77] S. K. Lee, Methods and apparatuses of lens flare rendering using linear paraxial approximation, and methods and apparatuses of lens flare rendering based on blending, U.S. Patent 2017/0140558 A1 (2017).